Supplementary Information (SI) for Energy & Environmental Science.
This journal is © The Royal Society of Chemistry 2024

1 **Electronic Supplementary Information**

2

3 Reducing carrier recombination loss by suppressing Sn loss 4 and defect formation via Ag doping in $Cu_2ZnSn(S,Se)_4$ solar 5 cells†

6

7 SeongYeon Kim,‡[a] Jaebaek Lee,[ab] Dae-Ho Son,[a] Wook Hyun Kim,[a] Shi-Joon Sung,[ab] Dae-Kue 8 Hwang,[ab] Tae Ei Hong,[c] Namuundari Otgontamir,[c] Enkhjargal Enkhbayar,[c] Tae-Hee Lee,[d] Min-Yeong 9 Kim,[d] Ji-Soo Choi,[d] Sang-Mo Koo,★[d] JunHo Kim,★[c] Jin-Kyu Kang,★[ab] Dae-Hwan Kim★[ab] and Kee-Jeong 10 Yang‡★[ab]

11

12 [a] Division of Energy & Environmental Technology, DGIST, Daegu 42988, Republic of Korea. E-mail: 13 apollon@dgist.ac.kr, monolith@dgist.ac.kr, kjyang@dgist.ac.kr

14 [b] Research Center for Thin Film Solar Cells, DGIST, Daegu 42988, Republic of Korea.

15 [c] Department of Physics, Incheon National University, Incheon 22012, Republic of Korea. E-mail: jhk@inu.ac.kr

16 [d] Department of Electronic Materials Engineering, Kwangwoon University, Seoul 01897, Republic of Korea. E-17 mail: smkoo@kw.ac.kr

18 † Electronic supplementary information (ESI) available. See DOI: https://doi.org/xxx

19 ‡ These authors contributed equally to this work.

20

21 **Keywords**

22 CZTSSe, Ag doping, sulfo-selenization mechanism, defects, Sn loss

1. Experimental

1.1 Solar cell fabrication

The CZTSSe solar cell device structure was composed of an SLG substrate, a Mo back contact, a CZTSSe absorber, a CdS buffer layer, a ZnO layer, an Al-doped ZnO (AZO) layer, and an Al grid (Fig. 1Sb, ESI†) The Mo back contact layer was deposited onto the SLG by direct current (DC) magnetron sputtering using a Mo target of 99.99% purity. Five precursor structures were designed and applied in this study: Sn/Cu/Zn/Mo/SLG (C1), Sn/Cu/Zn/Ag/Mo/SLG (C2), Sn/Cu/Ag/Zn/Mo/SLG (C3), Sn/Ag/Cu/Zn/Mo/SLG (C4), and Ag/Sn/Cu/Zn/Mo/SLG (C5). Metal precursors were deposited using 99.99% pure Cu, Zn, and Sn sputtering targets with 4-inch diameters and direct current (DC) sputtering powers of 150 W, 300 W, and 300 W, respectively, in an Ar atmosphere at a deposition pressure of 3 mTorr for Cu and 1 mTorr for Zn and Sn. The thicknesses achieved were 197, 249, and 291 nm. A Ag layer with a thickness of 5 nm was deposited using a thermal evaporator. Fig. S1a shows the profile of the sulfo-selenization process. For the sulfo-selenization process, all samples were placed in a jig consisting of a quartz boat, a sample holder made of SiC-coated graphite, and a quartz cover plate. H_2S gas diluted with 90 vol% Ar was used as the sulfur source, and Se pellets were used as the Se source. The Se pellets were purchased from Sigma–Aldrich and used without further purification. After introduction of 0.22 g Se pellets and injection of 250 sccm H_2S gas and 2000 sccm Ar gas into a rapid thermal processing (RTP) chamber, all gas supplies were stopped when the chamber pressure reached 700 Torr. The chamber was ramped from room temperature to 300°C for 550 s and maintained at 300°C

for 900 s. The chamber was then ramped from 300°C to 510°C for 1750 s and maintained at 510°C for 600 s. A 50-nm-thick CdS buffer layer was deposited via chemical bath deposition (CBD) using a bath containing cadmium sulfate ($CdSO_4$), ammonium hydroxide (NH_4OH), thiourea (NH_2CSNH_2), and DI H_2O. The solution was composed of 100 ml cadmium sulfate (0.015 M $CdSO_4$), 80 ml NH_4OH ammonium hydroxide, 50 ml thiourea (1.5 M NH_2CSNH_2), and 732 ml DI H_2O. The solution was heated under continuous stirring, and the temperature was maintained at 65℃ ± 1℃. The samples were deposited for 13 min and then cleaned using ultrasonication in DI H_2O. A 50-nm-thick intrinsic ZnO layer was deposited with a radio-frequency (RF) sputtering power of 150 W and a working pressure of 6 mTorr for 750 s. A 450-nm-thick Al-doped ZnO (AZO) layer was deposited with an RF sputtering power of 200 W and a working pressure of 2 mTorr at 200℃ for 3600 s. Finally, a 2.6-μm-thick Al collection grid was deposited on top of the device using thermal evaporation. The active area of the cell, excluding the Al grid area, was approximately 0.185 cm^2.

1.2 Device characterization

The current-voltage (*IV*) characteristics were determined under a simulated air mass with a 1.5 global (AM 1.5 G) spectrum and 100 mW cm^{-2} (1 sun) illumination at 25℃ using a 94022A solar simulator (Newport Co.). The external quantum efficiency (EQE) values were obtained using an SR 830 digital signal processor (DSP) lock-in amplifier system (McScience Co.). To investigate the

photoluminescence (PL) peak characteristics and carrier lifetime, PL and time-resolved photoluminescence (TRPL) measurements were conducted at room temperature using a compact near-infrared fluorescence lifetime spectrometer (C12132, Hamamatsu Co.) equipped with a YAG laser (532 nm). For the excitation laser line, the second harmonic of the YAG laser (532 nm) with a repetition frequency of 15 kHz was used. Temperature-dependent voltage characteristics were measured under white light illumination using a source meter (2400, Keithley Co.) under AM 1.5 G spectrum illumination with a 100 mW cm^{-2} (1 sun) Xe lamp (Abet Technology Co.) in the temperature range of 90–300 K. Admittance spectroscopy (AS) measurements were used to assess the energy levels of defects within the bandgaps of the CZTSSe absorber layer. These measurements were performed within the temperature range of 90–300 K using an E4980A LCR meter (Agilent Co.), in which probe frequencies from 20 Hz to 2 MHz were utilized. The measurements were conducted with a temperature tolerance of ± 0.05 K or less. To verify the defect activation energy (E_a), Arrhenius plots of the AS curve inflection points were constructed. To investigate deep-level defect characteristics, including the carrier capture cross section (σ) and defect density (N_{DLTS}), deep-level transient spectroscopy (DLTS) was performed using a custom system. N_{DLTS} was extracted from each peak of the DLTS spectra through an Arrhenius plot, and σ was extracted from the slope and y-intercept of the straight line connecting each point of the Arrhenius plot. Cross-sectional scanning transmission electron microscopy-energy dispersive spectroscopy (STEM-EDS) measurements were performed to analyze the elemental compositions and distributions near the absorber surfaces using a Themis S/TEM (Thermo Scientific

Co.). The elemental content was measured using a SuperXG2 EDS system attached to the TEM instrument. Elemental data were collected via a spectral imaging modality with a dwell time of 20 μs/pixel (pixel size: 4.725 nm). X-ray diffraction (XRD, Empyrean, PANalytical Co.) was performed using Cu Kα radiation (λ=0.15406 nm) to analyze the crystal structures of the precursors. For the five precursor structures, SLG/Mo/absorber samples were analyzed, and SLG/absorber samples were also analyzed to identify Ag-related peaks that overlapped with the Mo-related peaks. Raman spectroscopy measurements were performed using a custom Raman system equipped with a spectrometer (Mmac 750) and a laser with an excitation wavelength of λ = 532 nm (irradiation power < 1 mW) and a spot size of 0.7–1 μm. A 532 nm green laser was used with the power reduced to 1% by a Nd filter. The laser was focused on the surface of the sample through a 100x magnification lens, and measurements were performed under the conditions of an exposure time of 90 s and an accumulation count of 2. Each measurement was made by focusing the laser on the left, center, and right sides of the sample surface. Ultraviolet photoelectron spectroscopy (UPS) (ESCALAB 250Xi, Thermo Scientific Co.) was performed to measure the work function and valence band maximum on the surfaces of CZTSSe and CdS. SLG/Mo/absorber samples were used for CZTSSe characterization, and SLG/Mo/absorber/CdS samples were used for CdS characterization. Under ultrahigh vacuum conditions with a base pressure of 1×10^{-9} mbar, the samples were biased at -20 V. A He I (21.22 eV) ultraviolet source irradiated the samples, and the binding energy was measured in the range of -30 to 10 eV. At this time, the UPS spectra were calibrated with reference to the Fermi level of an electron beam-evaporated Au thin-film substrate.

1 To measure the bandgap energy of CdS, the absorbance (UV-2600, Shimadzu Co.) was measured in the

2 wavelength range of 300-1200 nm using SLG/CdS samples.

3

4 # 2. Results and discussion

5 ## 2.1 Characteristics of device with various Ag positions

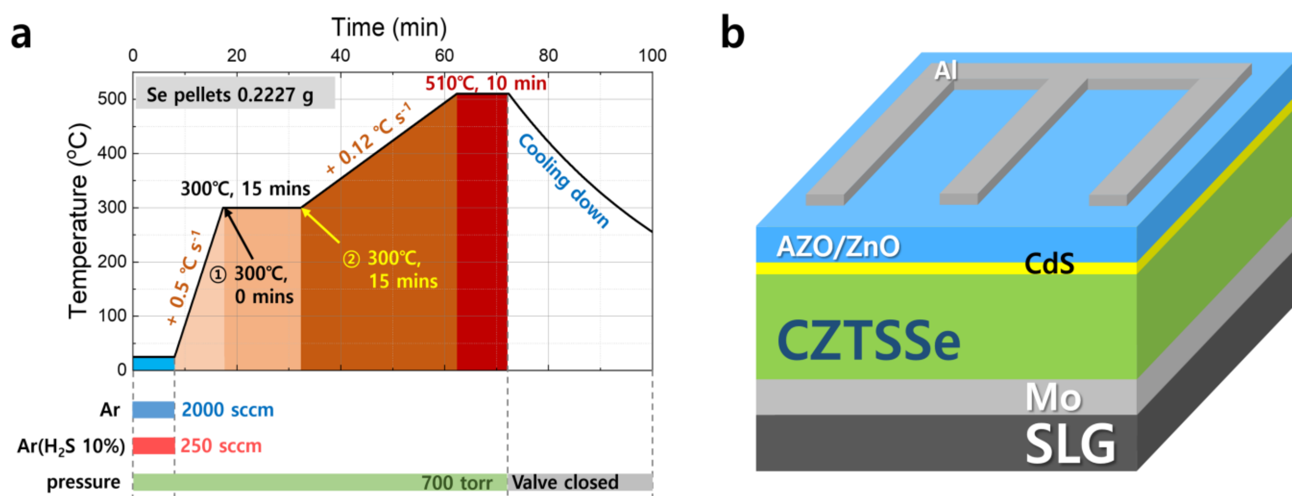

6

7 **Fig. S1** (a) Sulfo-selenization process conditions using RTP. (b) CZTSSe solar cell structure.

8

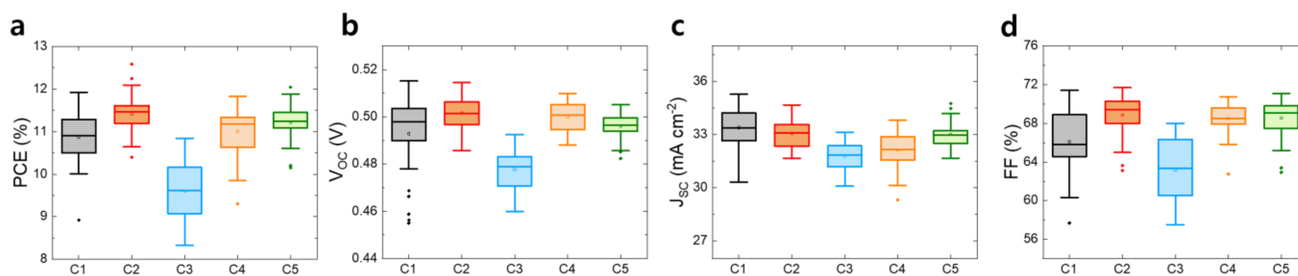

9

10 **Fig. S2** Properties of CZTSSe thin-film solar cells with various Ag layer positions. Boxplots of the (a) efficiency, (b) V_{OC}, (c)

11 J_{SC}, and (d) *FF* of 32 cells of each precursor type with a cell area of 0.185 cm^2.

12

1 **Table S1** Photovoltaic properties of CZTSSe solar cells for 32 cells of each precursor type

Sample		PCE (%)	V_{OC} (V)	J_{SC} (mA cm^{-2})	*FF* (%)
C1	Average	10.87	0.493	33.39	66.10
	Min.	8.92	0.455	30.32	57.69
	Max.	11.92	0.515	35.28	71.41
	StDev.	0.62	0.016	1.18	3.20
C2	Average	11.42	0.502	33.07	68.85
	Min.	10.39	0.486	31.67	63.13
	Max.	12.58	0.514	34.68	71.71
	StDev.	0.46	0.007	0.85	2.22
C3	Average	9.61	0.478	31.80	63.18
	Min.	8.33	0.460	30.09	57.53
	Max.	10.84	0.492	33.13	68.01
	StDev.	0.67	0.009	0.79	3.25
C4	Average	11.01	0.500	32.12	68.48
	Min.	9.31	0.488	29.32	62.75
	Max.	11.84	0.510	33.81	70.74
	StDev.	0.58	0.007	1.09	1.62
C5	Average	11.22	0.496	32.99	68.59
	Min.	10.15	0.482	31.67	62.93
	Max.	12.06	0.505	34.75	71.10
	StDev.	0.41	0.005	0.73	1.97

2

3

1

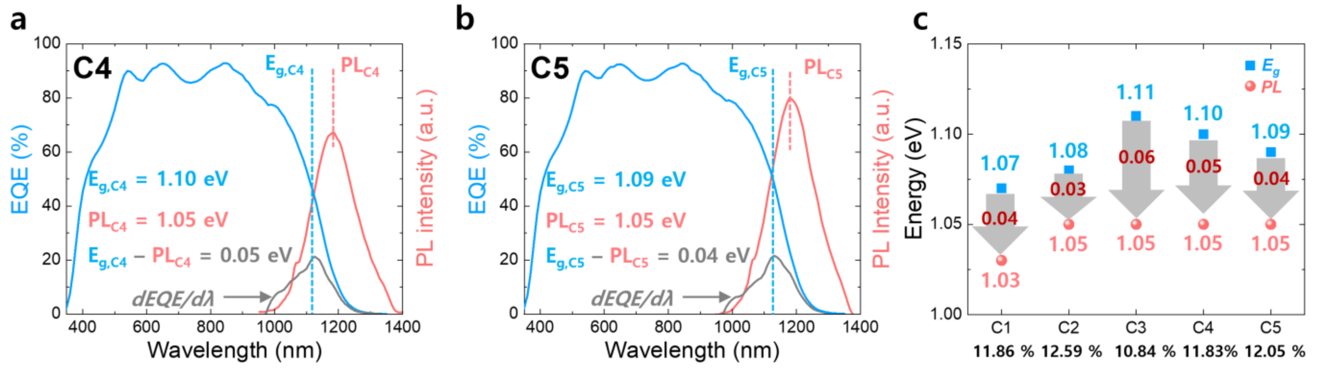

2 **Fig. S3** EQE curves at a bias of 0 V and PL spectra of the best-performing devices of (a) C4 and (b) C5. (c) E_g – PL shift
3 values for various Ag layer positions.

4

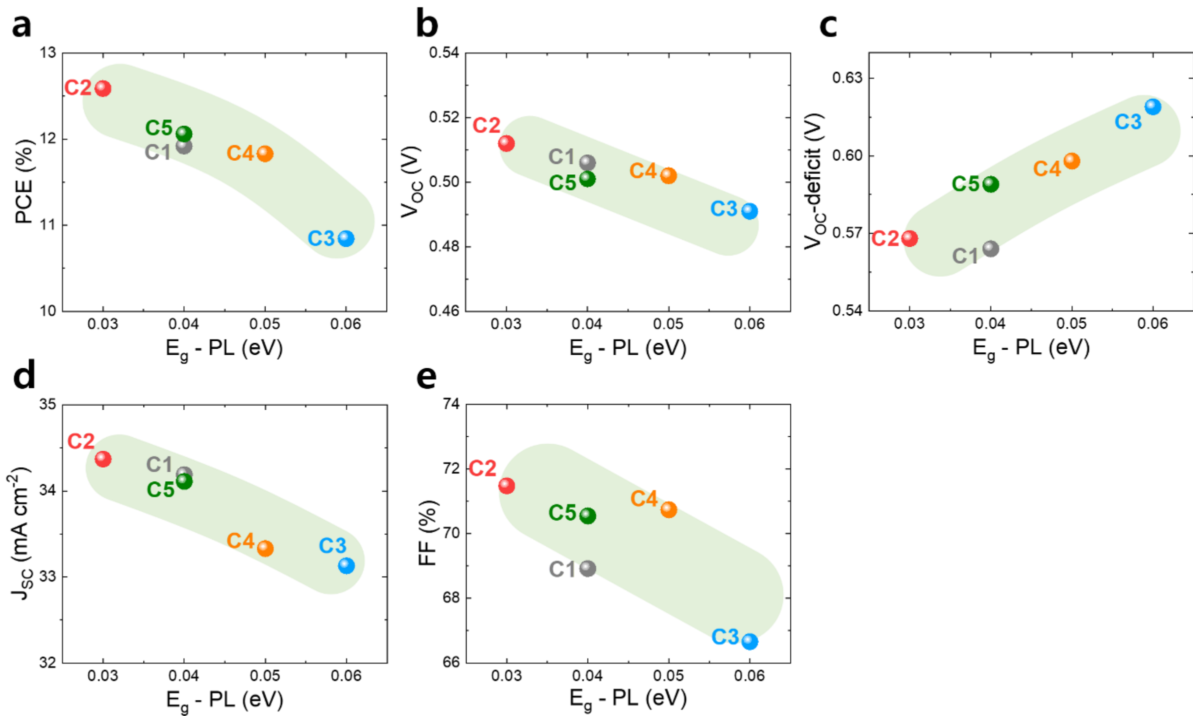

5

6 **Fig. S4** Relationships between E_g – PL and (a) PCE, (b) V_{OC}, (c) the V_{OC}-deficit, (d) J_{SC}, and (e) *FF*.

7

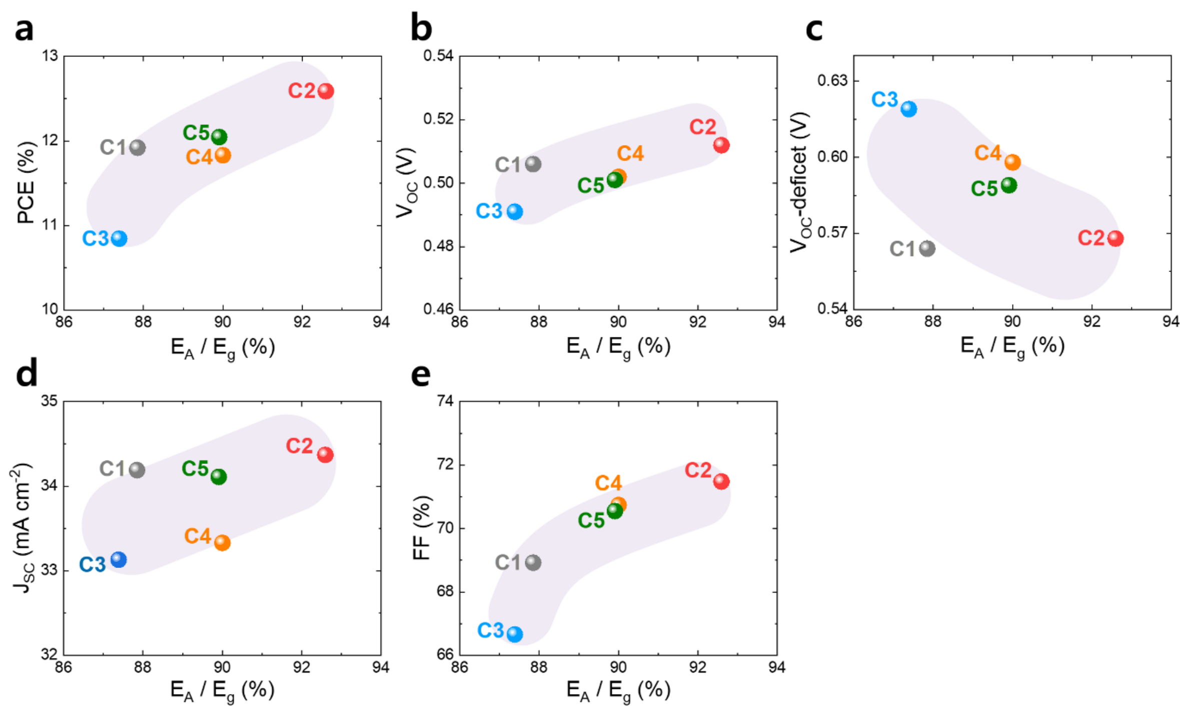

1

2 **Fig. S5** Relationships between E_A/E_g and (a) PCE, (b) V_{OC}, (c) the V_{OC}-deficit, (d) J_{SC}, and (e) *FF*.

3

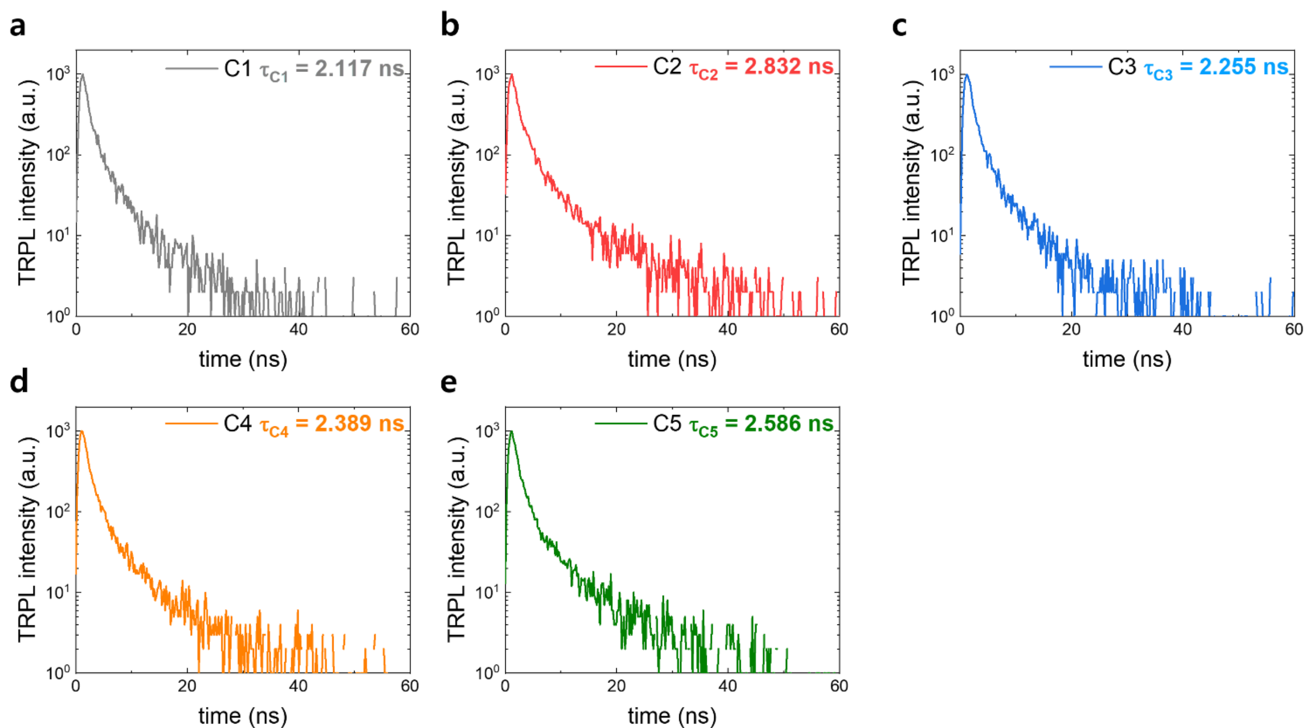

4

5 **Fig. S6** Carrier lifetimes of CZTSSe solar cells with various Ag layer positions.

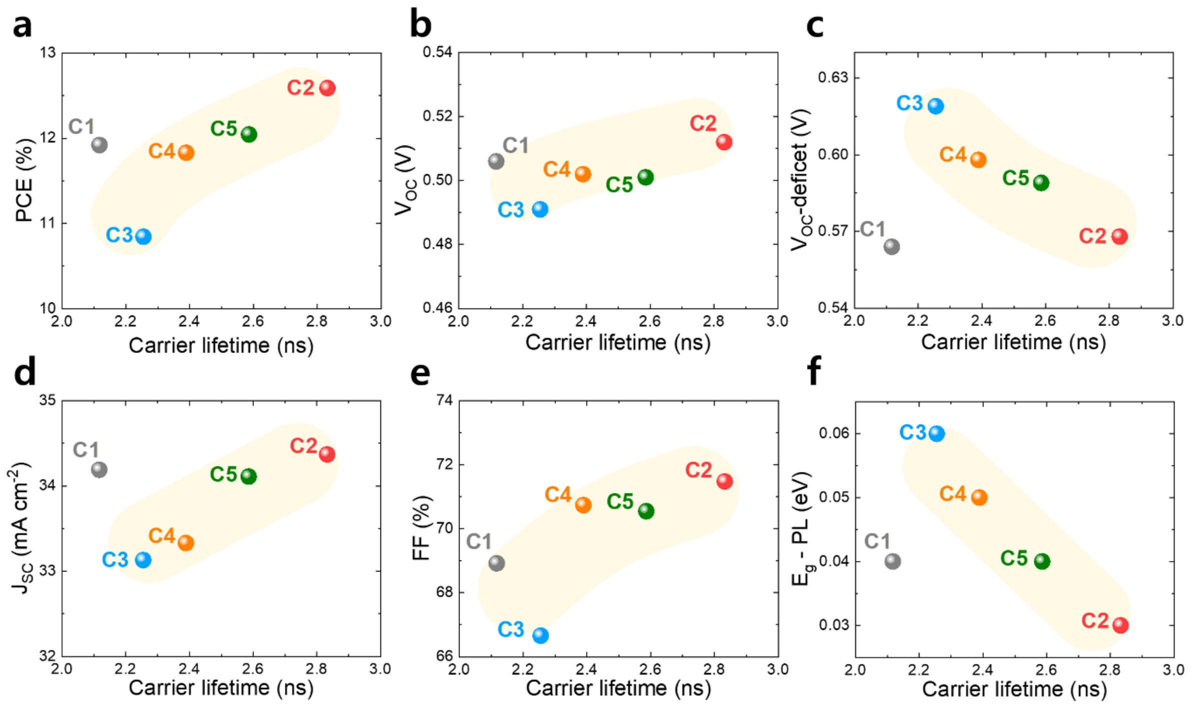

1

2 **Fig. S7** Relationships between the carrier lifetime and (a) PCE, (b) V_{OC}, (c) the V_{OC}-deficit, (d) J_{SC}, (e) FF, and (f) E_g – PL.

3

4

5

6

7

8

9

10

2.2 Defect characteristics for various Ag positions

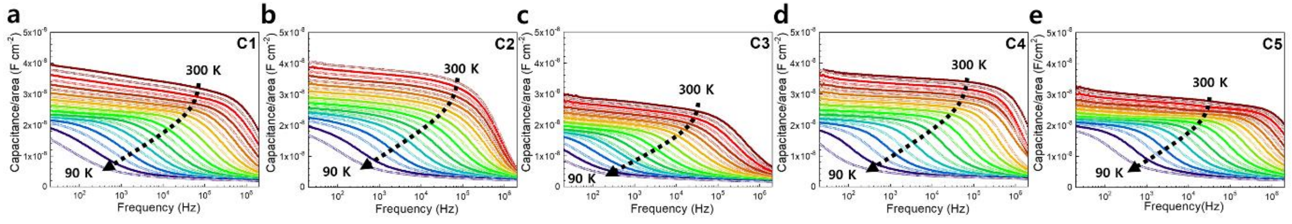

Fig. S8 AS spectra measured in the temperature range of 90 to 300 K using probe frequencies from 20 Hz to 2 MHz: (a) C1, (b) C2, (c) C3, (d) C4, and (e) C5.

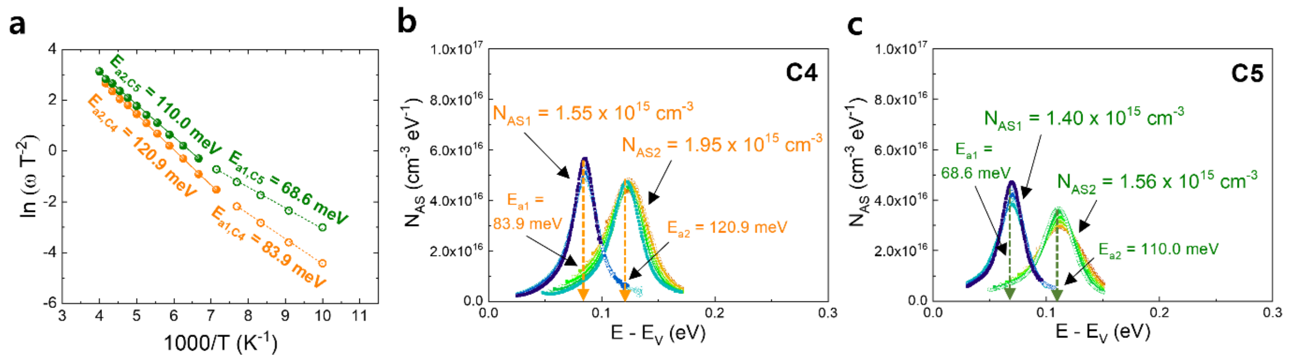

Fig. S9 (a) Arrhenius plots of the inflection points of the capacitance functions of C4 and C5, calculated from derivatives of the AS measurements (Fig. S8, ESI†). N_{AS} and E_a of (b) C4 and (c) C5, derived from the AS measurements.

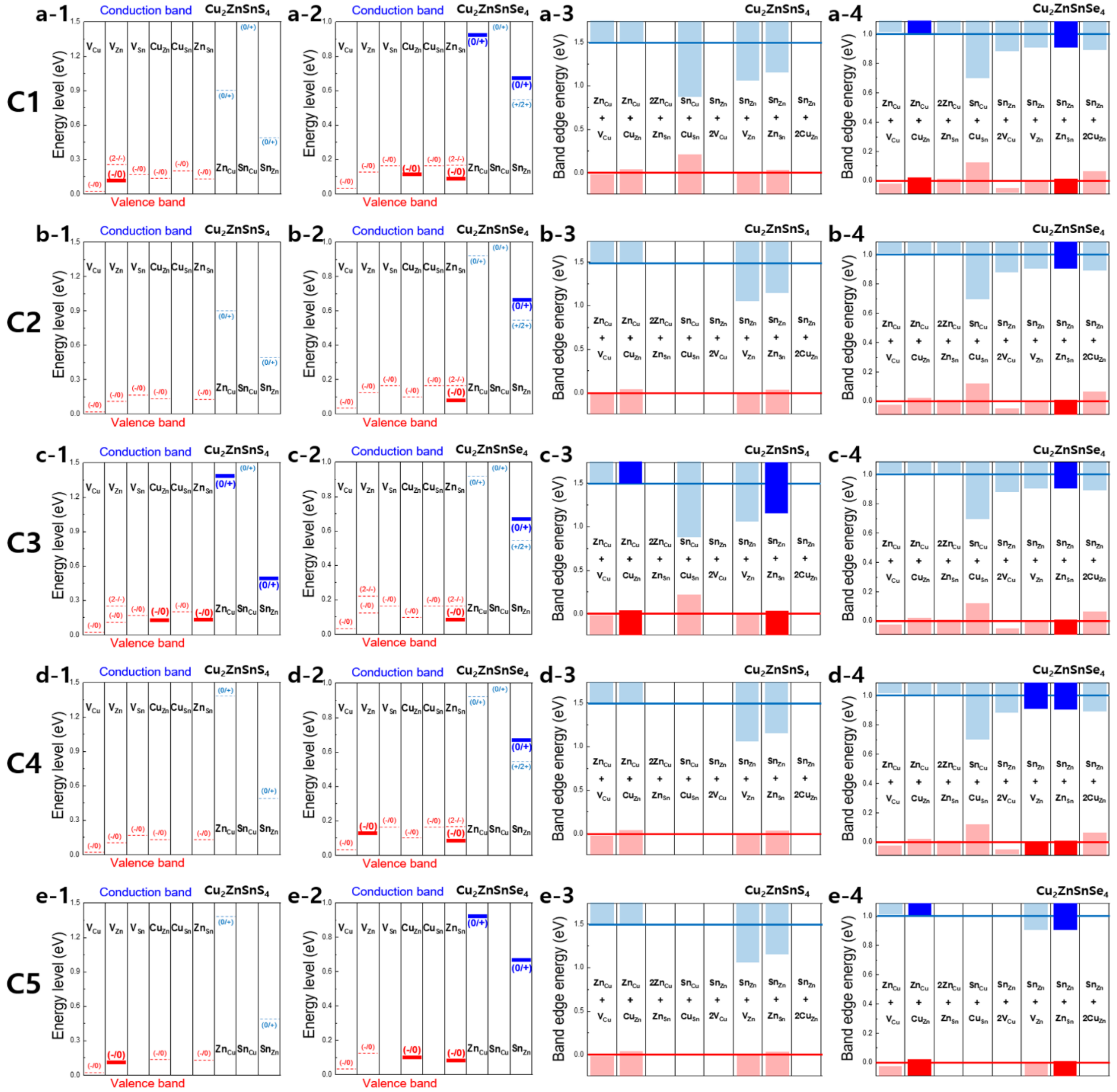

Fig. S10 Charged defects and defect clusters near the SCR for various Ag layer positions. (a) C1, (b) C2, (c) C3, (d) C4, and (e) C5. Defect energy levels near the SCRs of C1 ((a-1), (a-2)), C2 ((b-1), (b-2)), C3 ((c-1), (c-2)), C4 ((d-1), (d-2)), and C5 ((e-1), (e-2)). The thick solid line represents the main defects, and the dotted line represents defects that may exist within E_g. Defect clusters and band edge shifts near the SCRs of C1 ((a-3), (a-4)), C2 ((b-3), (b-4)), C3 ((c-3), (c-4)), C4 ((d-3), (d-4)), and C5 ((e-3), (e-4)). The dark color indicates the main defect cluster, and the light color indicates defect clusters that may exist within E_g.

1

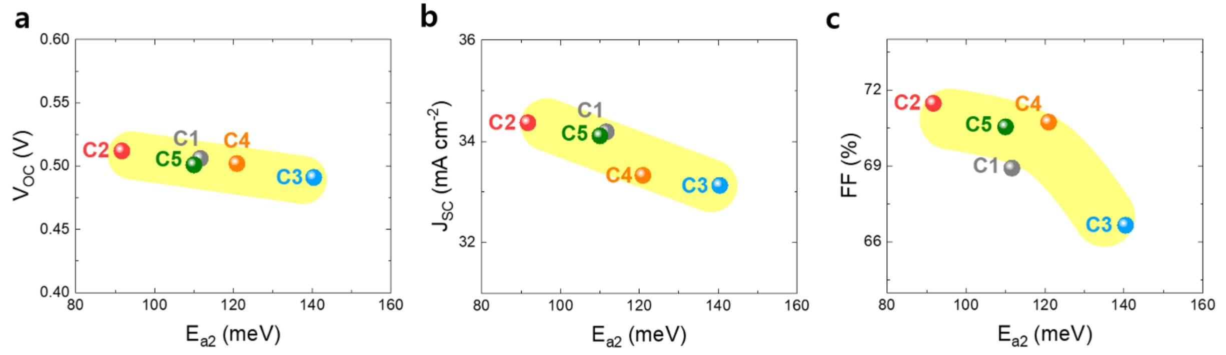

2 **Fig. S11** (a) Relationships between E_{a2} and (a) V_{OC}, (b) J_{SC}, and (c) FF.

3

4

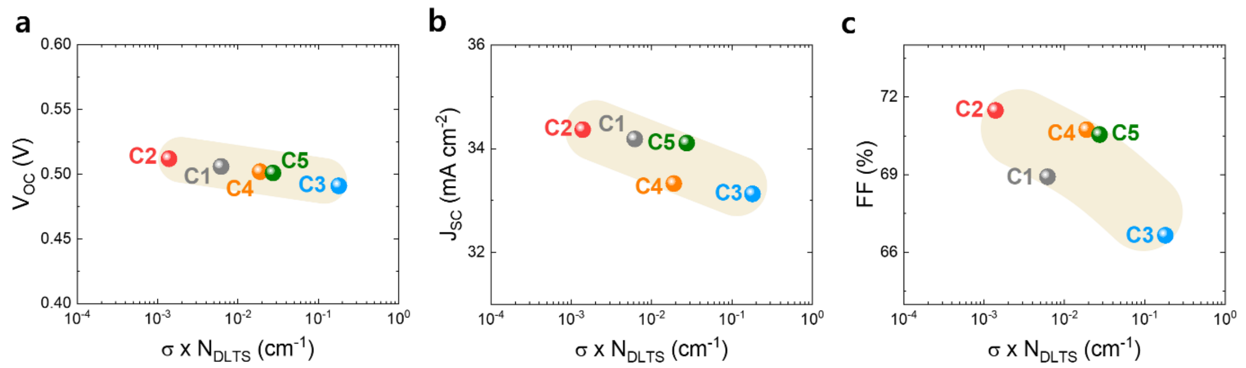

5 **Fig. S12** Relationships between σ x N_{DLTS} and (a) V_{OC}, (b) J_{SC}, and (c) FF.

6

7

8

9

10

11

12

13

14

15

2.3 Phases, elemental distributions, and sulfo-selenization mechanism for various Ag positions

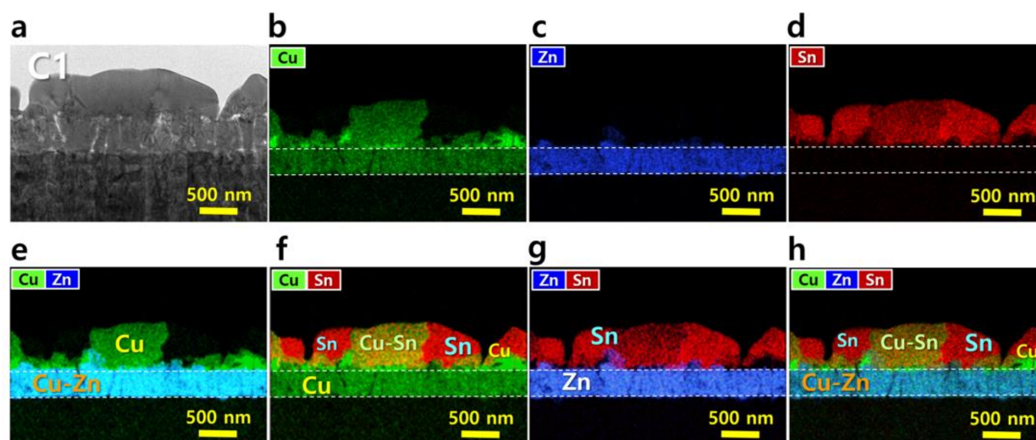

Fig. S13 Cross-sectional STEM-EDS mapping images of C1 after precursor deposition. (a) Cross-sectional STEM image. EDS mapping images of the C1 precursor showing the distributions of (b) Cu, (c) Zn, (d) Sn, (e) Cu and Zn, (f) Cu and Sn, (g) Zn and Sn, and (h) Cu, Zn, and Sn.

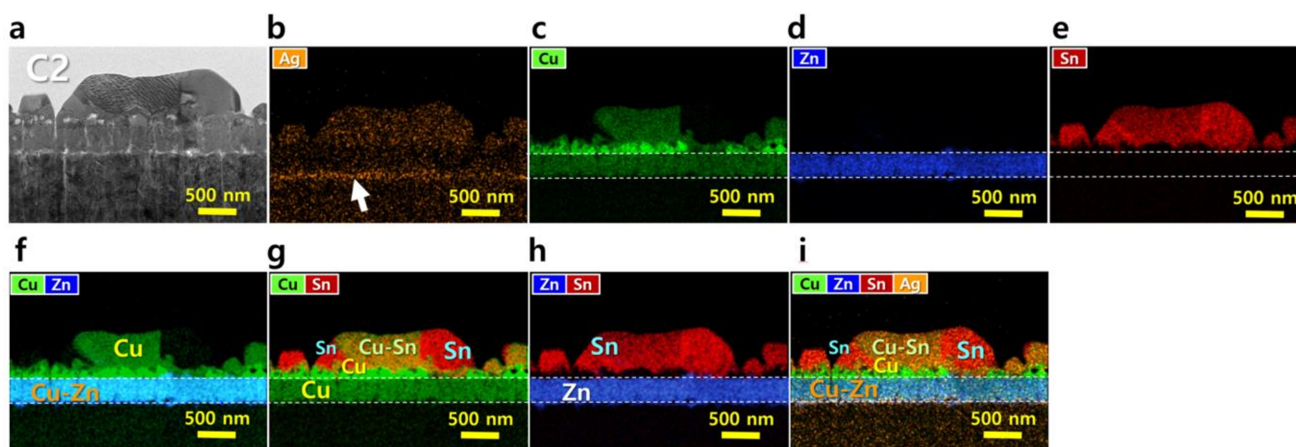

Fig. S14 Cross-sectional STEM-EDS mapping images of C2 after precursor deposition. (a) Cross-sectional STEM image. EDS mapping images of the C2 precursor showing the distributions of (b) Ag, (c) Cu, (d) Zn, (e) Sn, (f) Cu and Zn, (g) Cu and Sn, (h) Zn and Sn, and (i) Cu, Zn, Sn, and Ag.

1

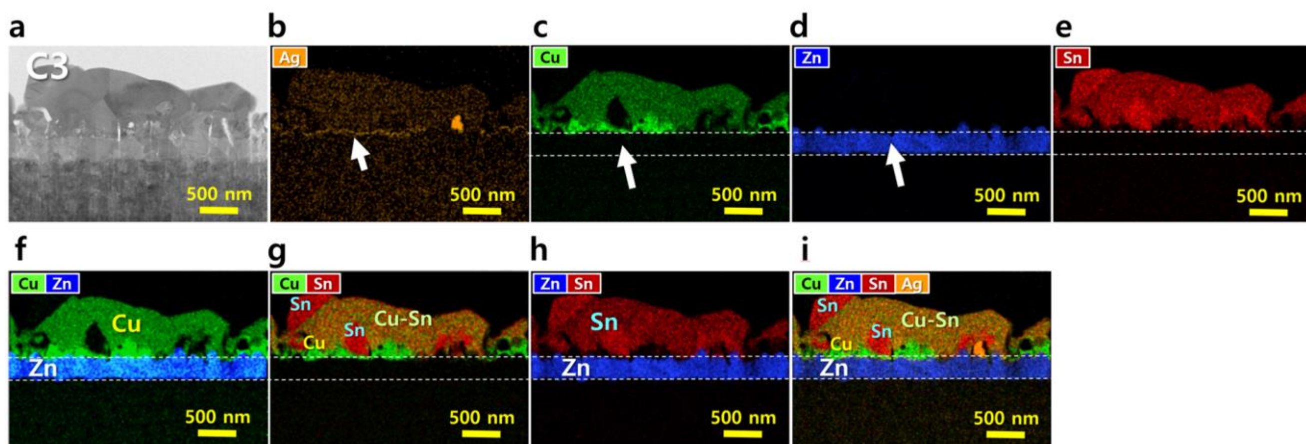

2 **Fig. S15** Cross-sectional STEM-EDS mapping images of C3 after precursor deposition. (a) Cross-sectional STEM image.
3 EDS mapping images of the C3 precursor showing the distributions of (b) Ag, (c) Cu, (d) Zn, (e) Sn, (f) Cu and Zn, (g) Cu and
4 Sn, (h) Zn and Sn, and (i) Cu, Zn, Sn, and Ag.

5

6

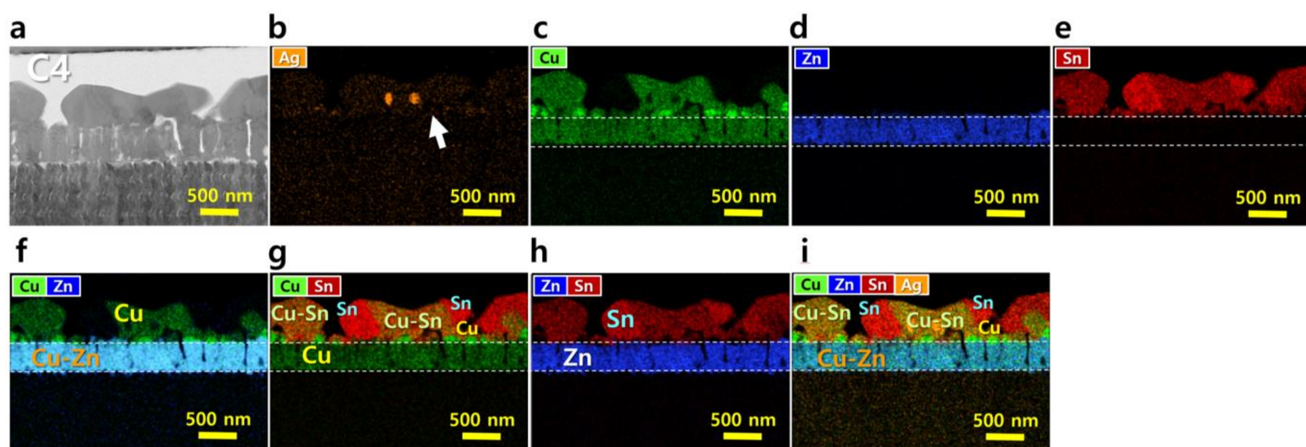

7 **Fig. S16** Cross-sectional STEM-EDS mapping images of C4 after precursor deposition. (a) Cross-sectional STEM image.
8 EDS mapping images of the C4 precursor showing the distributions of (b) Ag, (c) Cu, (d) Zn, (e) Sn, (f) Cu and Zn, (g) Cu and
9 Sn, (h) Zn and Sn, and (i) Cu, Zn, Sn, and Ag.

10

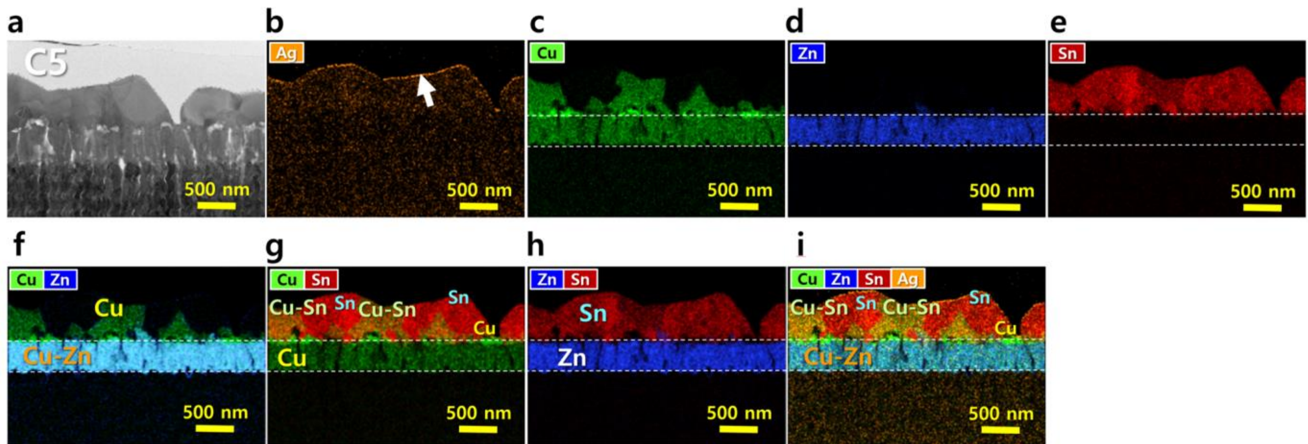

Fig. S17 Cross-sectional STEM-EDS mapping images of C5 after precursor deposition. (a) Cross-sectional STEM image. EDS mapping images of the C5 precursor showing the distributions of (b) Ag, (c) Cu, (d) Zn, (e) Sn, (f) Cu and Zn, (g) Cu and Sn, (h) Zn and Sn, and (i) Cu, Zn, Sn, and Ag.

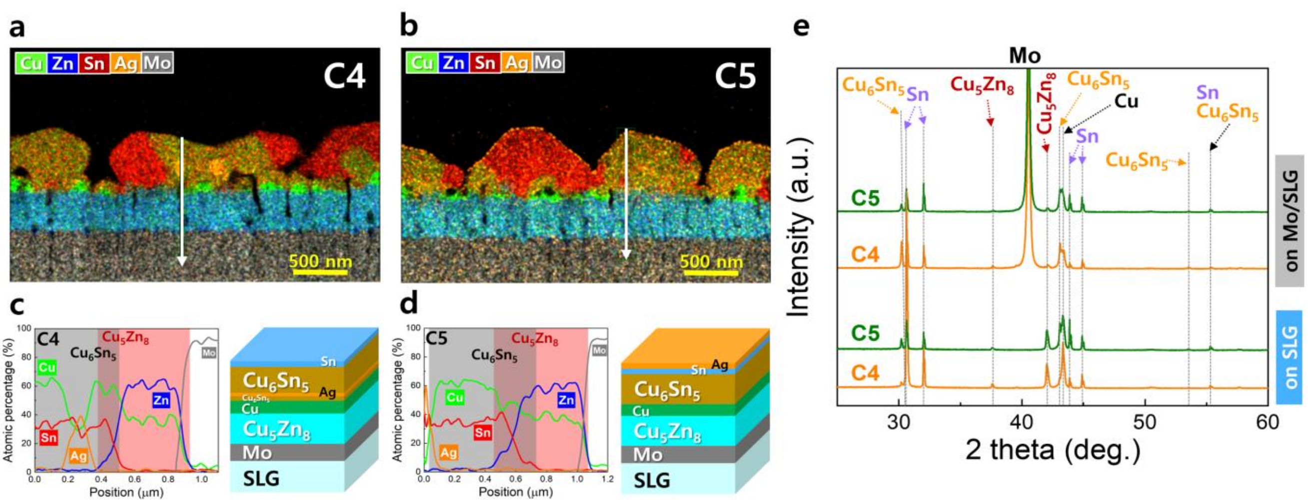

Fig. S18 Cross-sectional EDS maps of (a) C4 and (b) C5. Localized compositions and illustrations of the precursor phases of (c) C4 and (d) C5 determined using EDS line scans. The phase characteristics of the precursors are illustrated based on the localized composition results. (e) XRD patterns of C4 and C5 precursors on Mo/SLG and SLG.

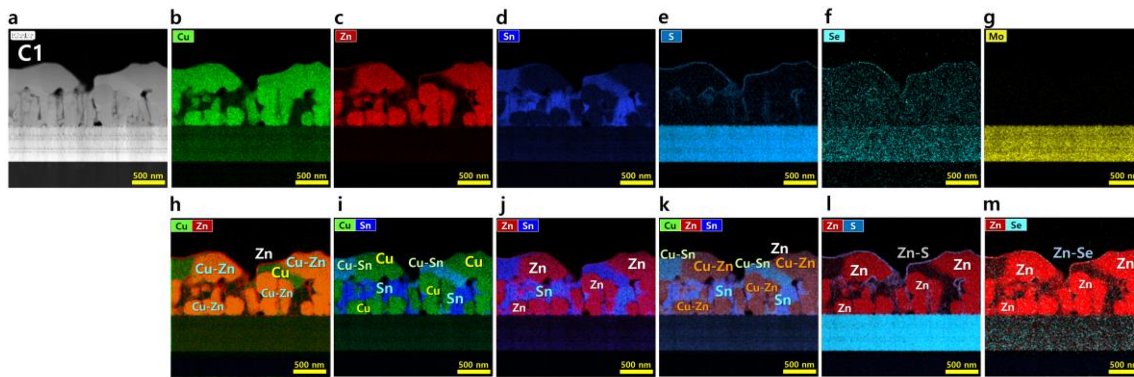

Fig. S19 Cross-sectional STEM-EDS mapping images of C1 after 0 min at 300°C during the sulfo-selenization process (Fig. S1a ①). (a) STEM image. EDS mapping images of the C1 precursor showing the distributions of (b) Cu, (c) Zn, (d) Sn, (e) S, (f) Se, (g) Mo, (h) Cu and Zn, (i) Cu and Sn, (j) Zn and Sn, (k) Cu, Zn, and Sn, (l) Zn and S, and (m) Zn and Se.

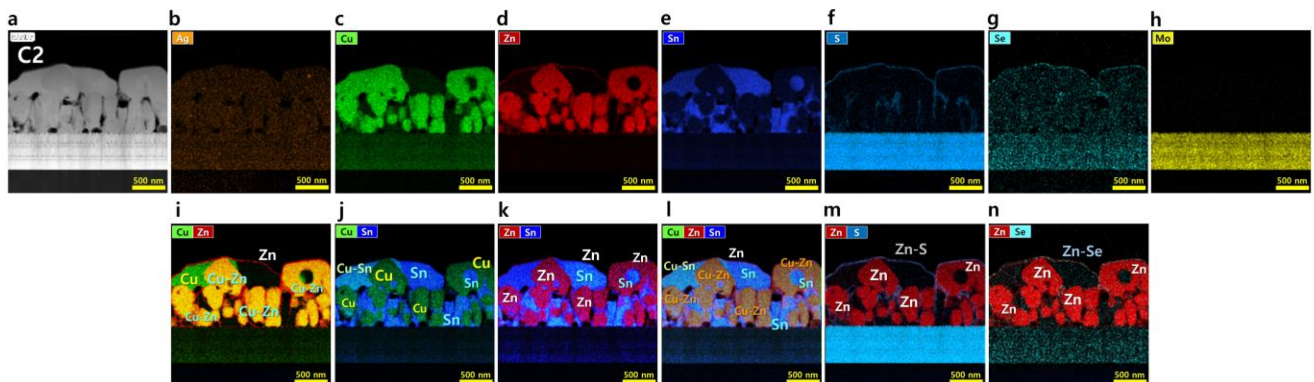

Fig. S20 Cross-sectional STEM-EDS mapping images of C2 after 0 min at 300°C during the sulfo-selenization process (Fig. S1a ①). (a) STEM image. EDS mapping images of the C2 precursor showing the distributions of (b) Ag, (c) Cu, (d) Zn, (e) Sn, (f) S, (g) Se, (h) Mo, (i) Cu and Zn, (j) Cu and Sn, (k) Zn and Sn, (l) Cu, Zn, and Sn, (m) Zn and S, and (n) Zn and Se.

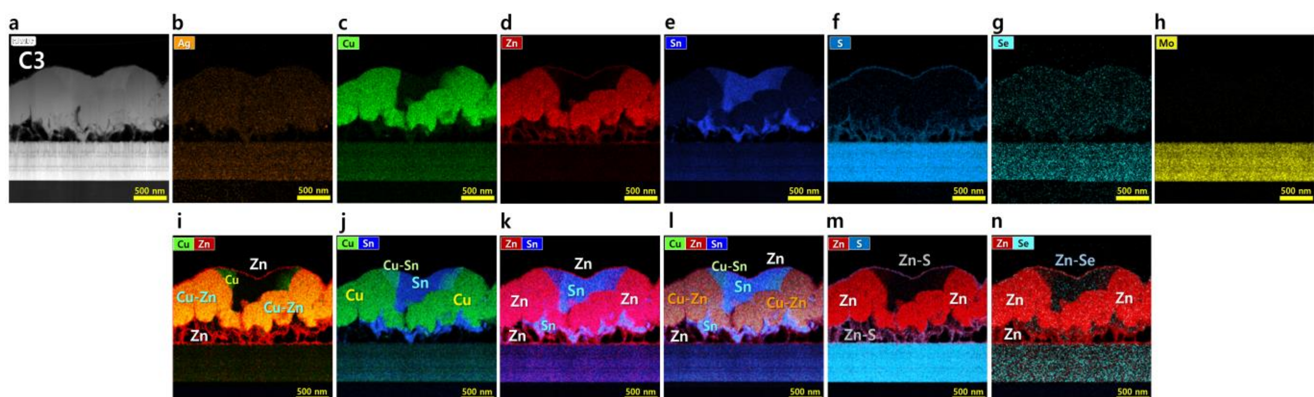

Fig. S21 Cross-sectional STEM-EDS mapping images of C3 after 0 min at 300°C during the sulfo-selenization process (Fig. S1a ①). (a) STEM image. EDS mapping images of the C3 precursor showing the distributions of (b) Ag, (c) Cu, (d) Zn, (e) Sn, (f) S, (g) Se, (h) Mo, (i) Cu and Zn, (j) Cu and Sn, (k) Zn and Sn, (l) Cu, Zn, and Sn, (m) Zn and S, and (n) Zn and Se.

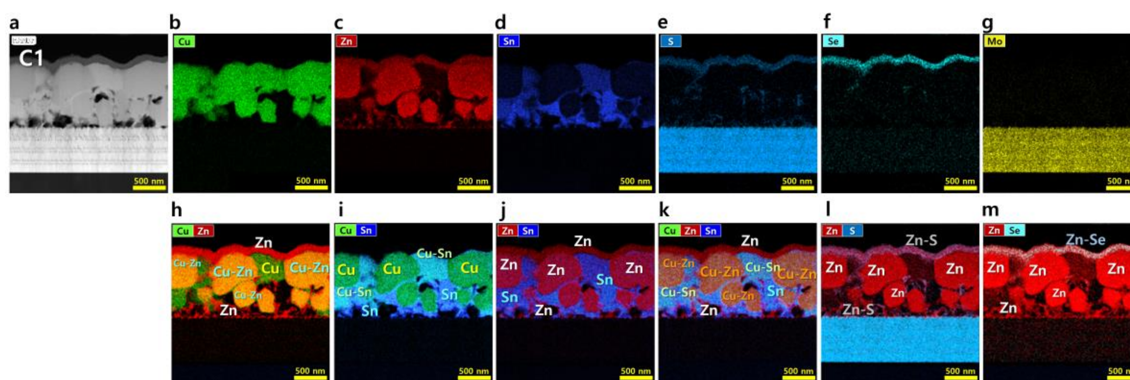

Fig. S22 Cross-sectional STEM-EDS mapping images of C1 after 15 min at 300°C during the sulfo-selenization process (Fig. S1a ②). (a) STEM image. EDS mapping images of the C1 precursor showing the distributions of (b) Cu, (c) Zn, (d) Sn, (e) S, (f) Se, (g) Mo, (h) Cu and Zn, (i) Cu and Sn, (j) Zn and Sn, (k) Cu, Zn, and Sn, (l) Zn and S, and (m) Zn and Se.

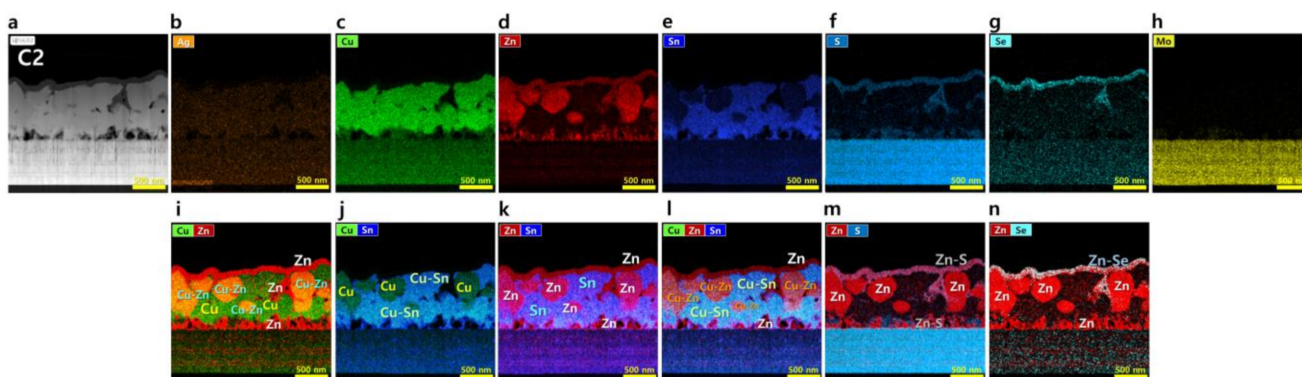

Fig. S23 Cross-sectional STEM-EDS mapping images of C2 after 15 min at 300°C during the sulfo-selenization process (Fig. S1a ②). (a) STEM image. EDS mapping images of the C2 precursor showing the distributions of (b) Ag, (c) Cu, (d) Zn, (e) Sn, (f) S, (g) Se, (h) Mo, (i) Cu and Zn, (j) Cu and Sn, (k) Zn and Sn, (l) Cu, Zn, and Sn, (m) Zn and S, and (n) Zn and Se.

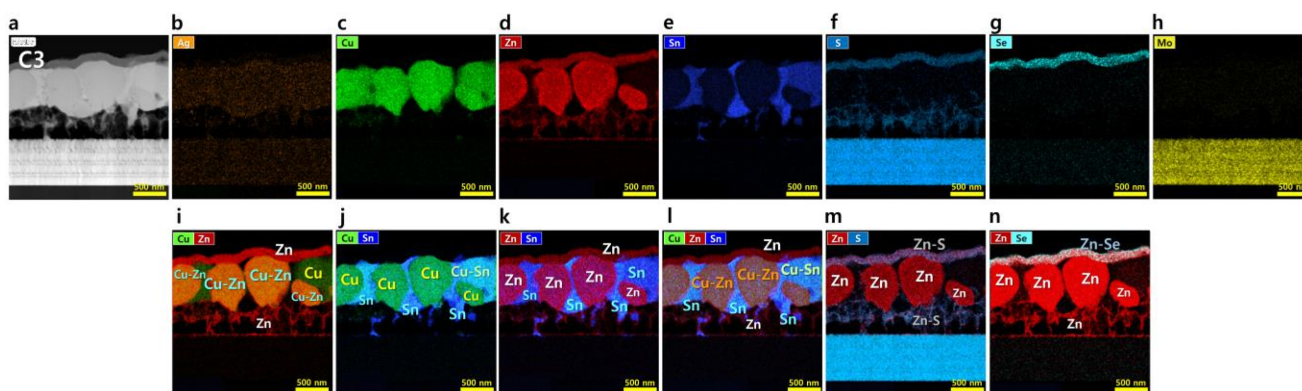

Fig. S24 Cross-sectional STEM-EDS mapping images of C3 after 15 min at 300°C during the sulfo-selenization process (Fig. S1a ②). (a) STEM image. EDS mapping images of the C3 precursor showing the distributions of (b) Ag, (c) Cu, (d) Zn, (e) Sn, (f) S, (g) Se, (h) Mo, (i) Cu and Zn, (j) Cu and Sn, (k) Zn and Sn, (l) Cu, Zn, and Sn, (m) Zn and S, and (n) Zn and Se.

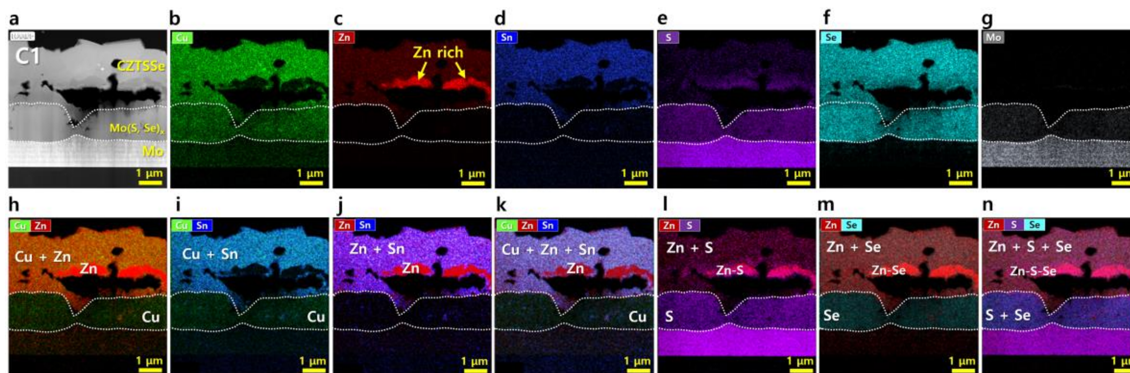

Fig. S25 Cross-sectional STEM-EDS mapping images of the C1 absorber after the sulfo-selenization process. (a) STEM image. EDS mapping images of the C1 absorber showing the distributions of (b) Cu, (c) Zn, (d) Sn, (e) S, (f) Se, (g) Mo, (h) Cu and Zn, (i) Cu and Sn, (j) Zn and Sn, (k) Cu, Zn, and Sn, (l) Zn and S, (m) Zn and Se, and (n) Zn, S, and Se.

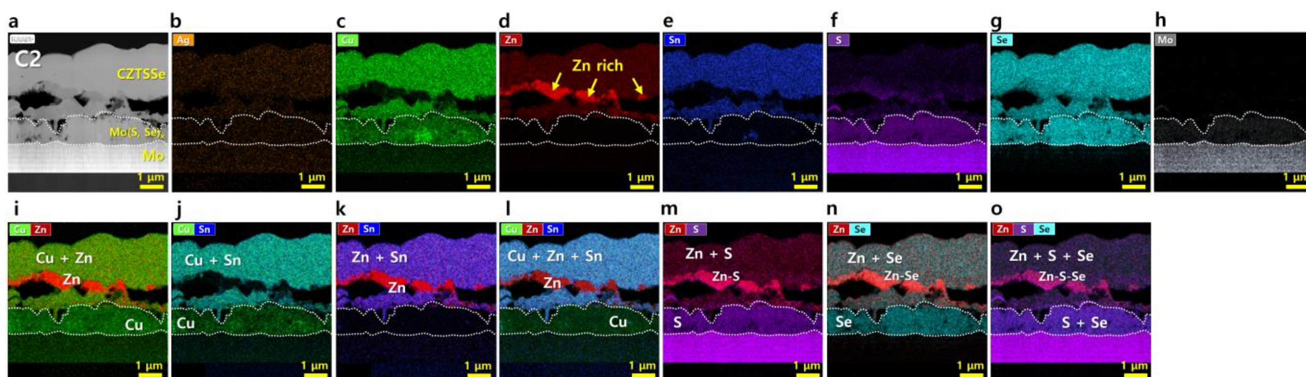

Fig. S26 Cross-sectional STEM-EDS mapping images of the C2 absorber after the sulfo-selenization process. (a) STEM image. EDS mapping images of the C2 absorber showing the distributions of (b) Ag, (c) Cu, (d) Zn, (e) Sn, (f) S, (g) Se, (h) Mo, (i) Cu and Zn, (j) Cu and Sn, (k) Zn and Sn, (l) Cu, Zn, and Sn, (m) Zn and S, (n) Zn and Se, and (o) Zn, S, and Se.

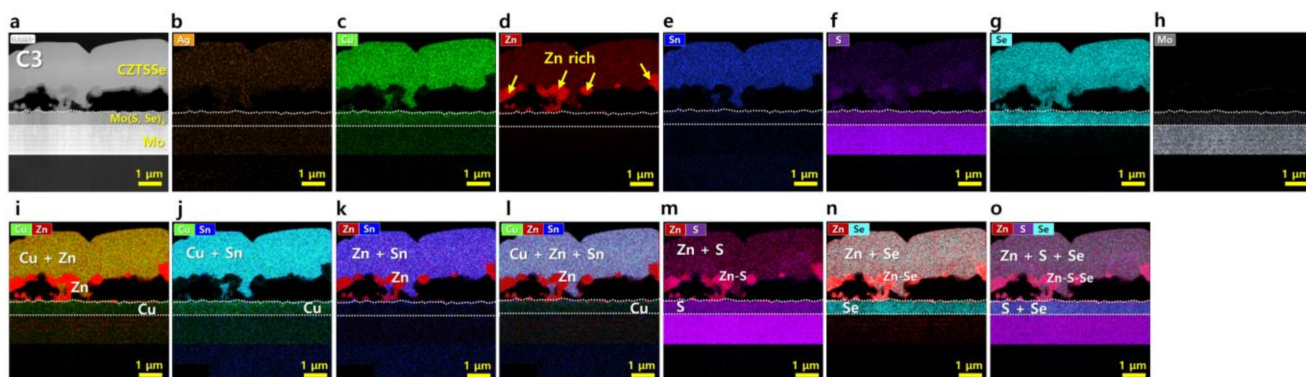

Fig. S27 Cross-sectional STEM-EDS mapping images of the C3 absorber after the sulfo-selenization process. (a) STEM image. EDS mapping images of the C3 absorber showing the distributions of (b) Ag, (c) Cu, (d) Zn, (e) Sn, (f) S, (g) Se, (h) Mo, (i) Cu and Zn, (j) Cu and Sn, (k) Zn and Sn, (l) Cu, Zn, and Sn, (m) Zn and S, (n) Zn and Se, and (o) Zn, S, and Se.

1

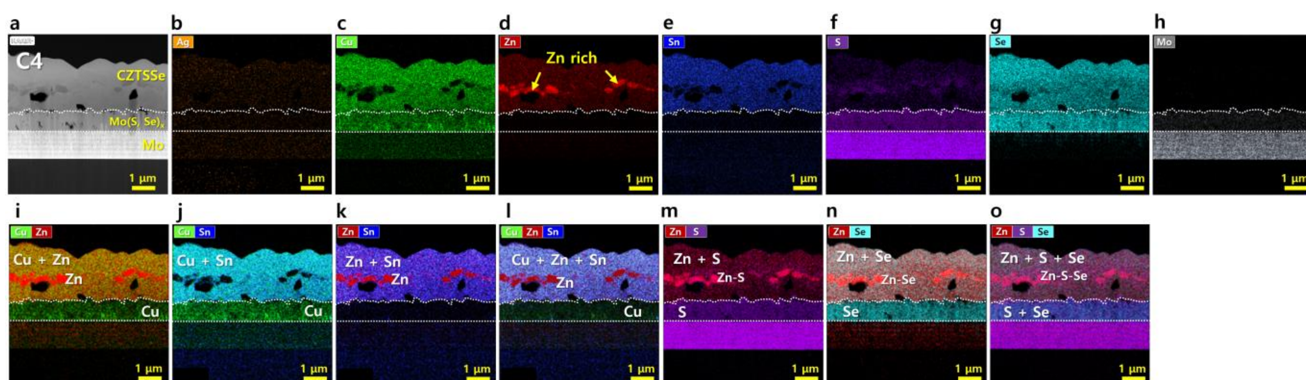

2 **Fig. S28** Cross-sectional STEM-EDS mapping images of the C4 absorber after the sulfo-selenization process. (a) STEM
3 image. EDS mapping images of the C4 absorber showing the distributions of (b) Ag, (c) Cu, (d) Zn, (e) Sn, (f) S, (g) Se, (h)
4 Mo, (i) Cu and Zn, (j) Cu and Sn, (k) Zn and Sn, (l) Cu, Zn, and Sn, (m) Zn and S, (n) Zn and Se, and (o) Zn, S, and Se.

5

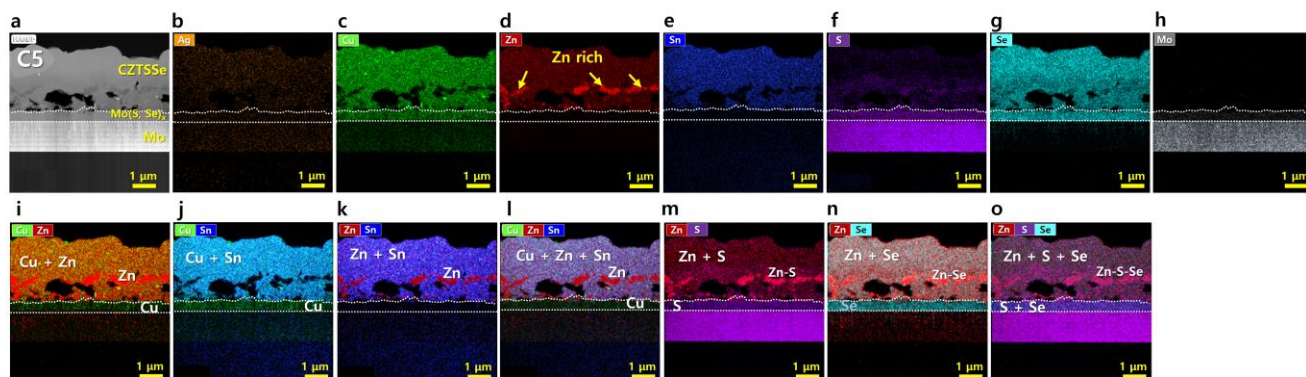

6 **Fig. S29** Cross-sectional STEM-EDS mapping images of the C5 absorber after the sulfo-selenization process. (a) STEM
7 image. EDS mapping images of the C5 absorber showing the distributions of (b) Ag, (c) Cu, (d) Zn, (e) Sn, (f) S, (g) Se, (h)
8 Mo, (i) Cu and Zn, (j) Cu and Sn, (k) Zn and Sn, (l) Cu, Zn, and Sn, (m) Zn and S, (n) Zn and Se, and (o) Zn, S, and Se.

9

1

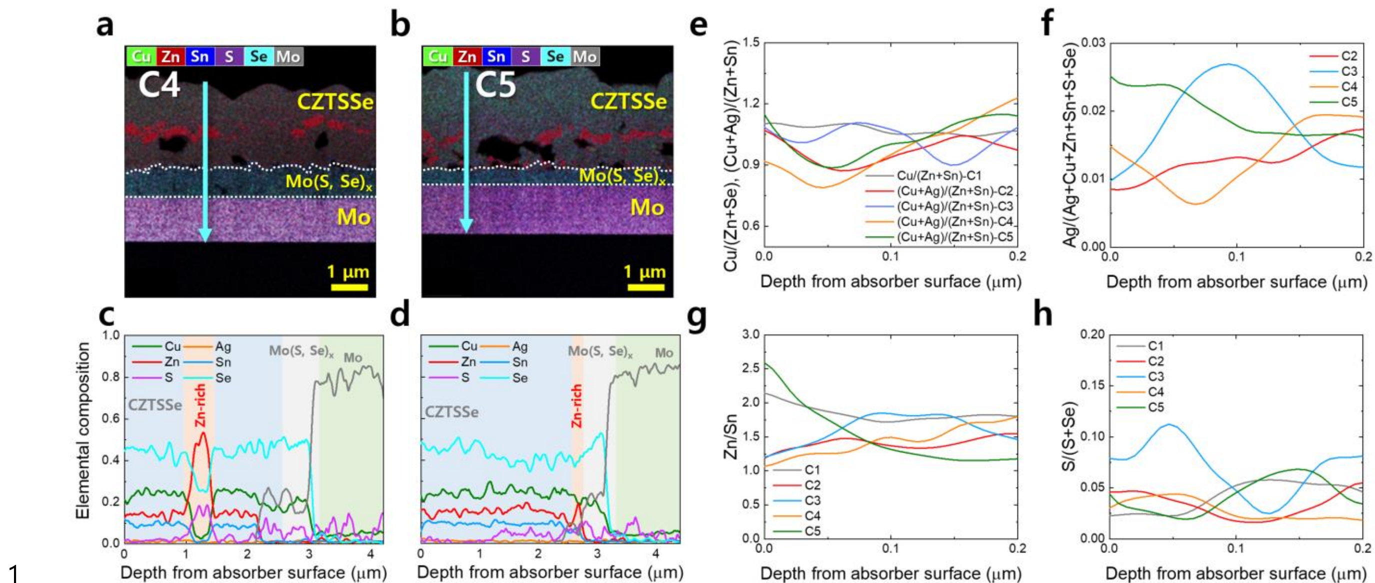

2 **Fig. S30** Cross-sectional EDS mapping images of the (a) C4 and (b) C5 absorbers after the sulfo-selenization process.
3 Localized elemental distributions in the (c) C4 and (d) C5 absorbers obtained using EDS line scans. Elemental ratio variations
4 of (e) Cu/(Zn+Sn) and (Cu+Ag)/(Zn+Sn), (f) Ag/(Cu+Zn+Sn+S+Se), (g) Zn/Sn, and (h) S/(S+Se) in C1, C2, C3, C4, and C5
5 from the absorber surface to a depth of 0.2 μm.

6

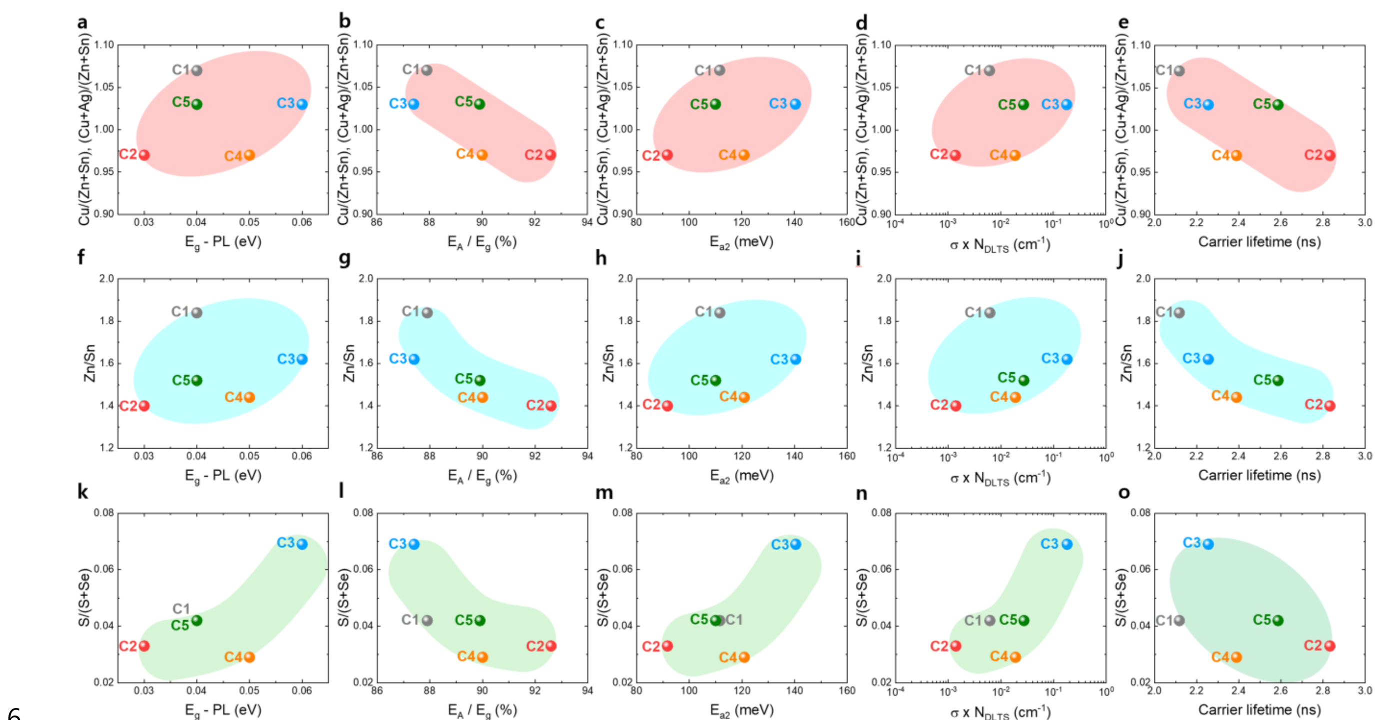

7 **Fig. S31** Relationships between the average elemental ratio from the absorber surface to a depth of 0.2 μm and E_g – PL,
8 E_A/E_g, E_{a2}, σ x N_{DLTS}, and the carrier lifetime.

1

Table S2 S/(S+Se) ratio variation data for C1–C5 from the absorber surface to a depth of 0.2 μm

S/(S+Se)	C1	C2	C3	C4	C5
Average	0.042	0.033	0.069	0.029	0.042
Min.	0.023	0.016	0.025	0.018	0.019
Max.	0.058	0.055	0.112	0.044	0.068
Max. – Min.	0.035	0.039	0.088	0.026	0.049
Median	0.049	0.034	0.078	0.022	0.040
StDev	0.014	0.012	0.026	0.010	0.017

2

3

Table S3 Ag/(Cu+Zn+Sn+S+Se) ratio variation data for C2–C5 from the absorber surface to a depth of 0.2 μm

Ag/(Ag+Cu+Zn+Sn+S+Se)	C2	C3	C4	C5
Average	0.013	0.018	0.013	0.020
Min.	0.008	0.010	0.006	0.06
Max.	0.017	0.027	0.019	0.025
Max. – Min.	0.009	0.017	0.013	0.009
Median	0.013	0.018	0.013	0.018
StDev	0.003	0.006	0.005	0.003

4

5

6

7

8

9

10

11

12

13

2.4 Band structure at the absorber–CdS interface for various Ag positions

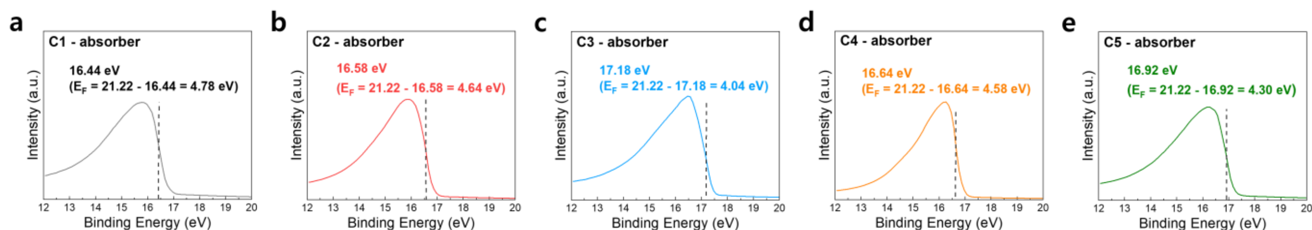

Fig. S32 E_F from the vacuum level (work function) of CZTSSe in the SLG/Mo/absorber samples with various Ag layer positions measured by UPS.

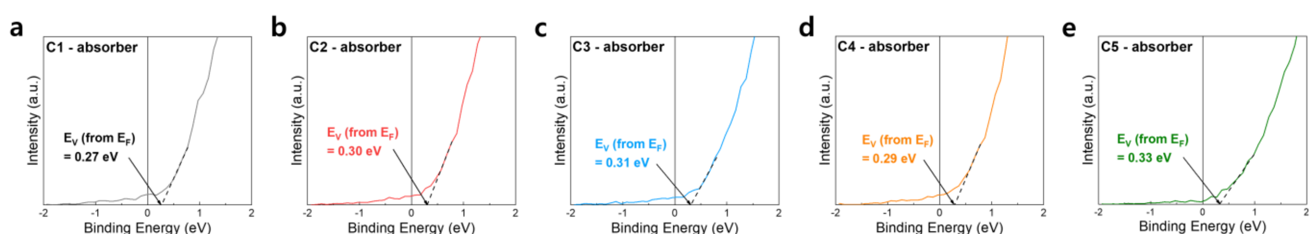

Fig. S33 E_F relative to E_V in the SLG/Mo/absorber samples with various Ag layer positions from the UPS results of CZTSSe.

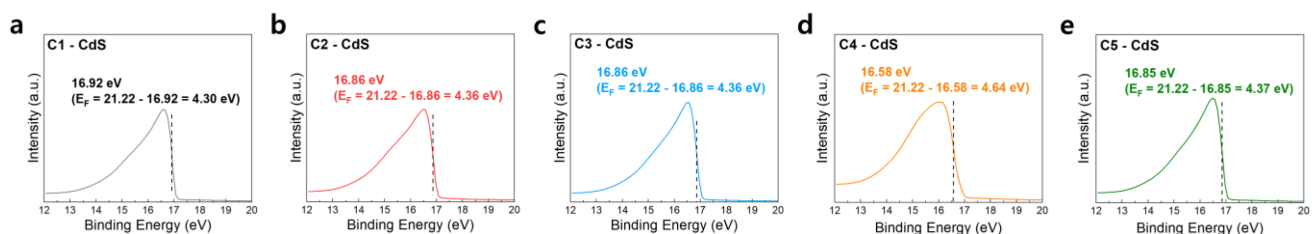

Fig. S34 E_F from the vacuum level (work function) of CdS in the SLG/Mo/absorber/CdS samples with various Ag layer positions measured by UPS.

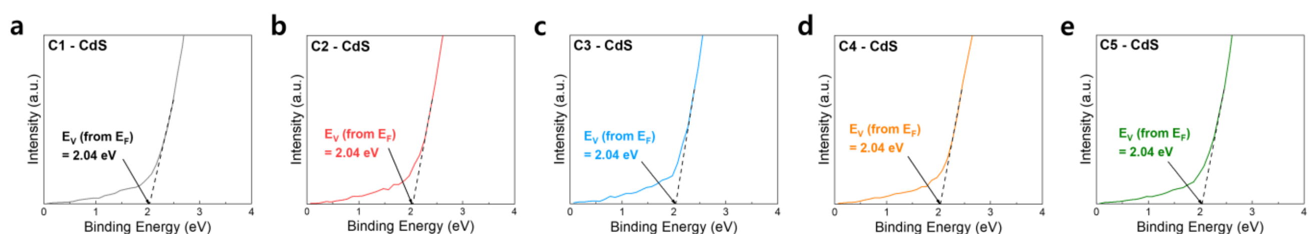

Fig. S35 E_F relative to E_V in the SLG/Mo/absorber/CdS samples with various Ag layer positions from the UPS results of CdS.

1

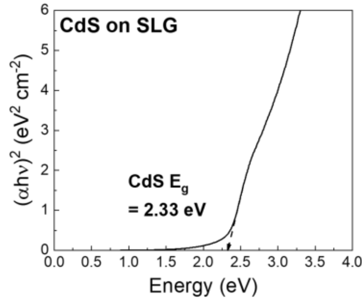

2 **Fig. S36** E_g of CdS in the SLG/CdS sample determined using the UV–Vis absorption spectrum.

3

4 **Table S4** Summary of the E_F, E_V, E_C, and E_g of CZTSSe and CdS with various Ag layer positions measured via UPS

Sample		E_F from vacuum level (work function) (eV)	E_V from E_F (eV)	E_V from vacuum level (eV)	E_g (eV)	E_C from vacuum level (eV)
C1	absorber	-4.78	-0.27	-5.05	1.07	-3.98
	CdS	-4.30	-2.04	-6.34	2.33	-4.01
C2	absorber	-4.64	-0.30	-4.94	1.08	-3.86
	CdS	-4.36	-2.04	-6.40	2.33	-4.07
C3	absorber	-4.04	-0.31	-4.35	1.11	-3.24
	CdS	-4.36	-2.04	-6.40	2.33	-4.07
C4	absorber	-4.58	-0.29	-4.87	1.10	-3.77
	CdS	-4.64	-2.04	-6.68	2.33	-4.35
C5	absorber	-4.30	-0.33	-4.63	1.09	-3.54
	CdS	-4.37	-2.04	-6.41	2.33	-4.08

5

1

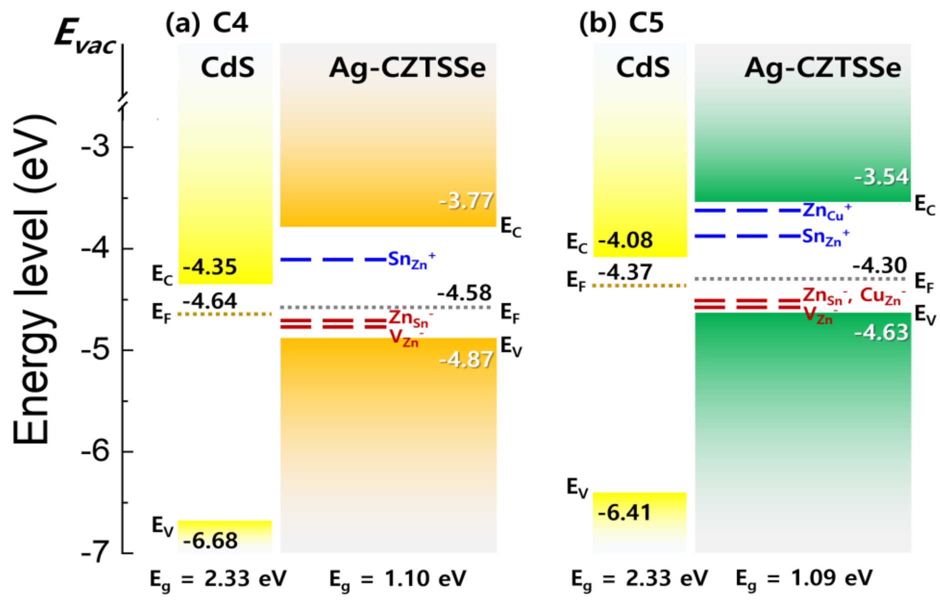

2 **Fig. S37** Schematic band alignment of the energy levels and defect energy levels of (a) C4 and (b) C5 at the CZTSSe–CdS

3 interface.